Faraday Discussions

Cite this: *Faraday Discuss.*, 2022, **239**, 273

ROYAL SOCIETY OF CHEMISTRY

PAPER

View Article Online
View Journal | View Issue

# A post-deposition annealing approach for organic residue control in $TiO_2$ and its impact on $Sb_2Se_3/TiO_2$ device performance

Mykhailo Koltsov,*[a] Robert Krautmann,[a] Atanas Katerski,[a] Natalia Maticiuc,[b] Malle Krunks,[a] Ilona Oja Acik[a] and Nicolae Spalatu*[a]

Received 21st March 2022, Accepted 31st March 2022
DOI: 10.1039/d2fd00064d

We report a systematic investigation on the influence of two-step post-deposition treatments (PDTs) on $TiO_2$ buffer layers deposited by ultrasonic spray pyrolysis (USP) for emerging $Sb_2Se_3$ photovoltaics. Air annealing is a typical method for recrystallizing chemically deposited $TiO_2$ films. However, organic residues (such as carbon species) from a precursor solution based on titanium tetraisopropoxide and acetylacetone may still remain on the $TiO_2$ surface, therefore requiring an additional annealing step. We demonstrate that vacuum annealing can be a suitable technological approach to decrease the concentration of carbon species in $TiO_2$ films. Vacuum annealing was performed at temperatures at 160–450 °C prior to the 450 °C air annealing step. It was found that vacuum annealing at 160 °C followed by subsequent air annealing led to better device performance. This was explained by achieving an optimal balance between the removal of carbon content during vacuum annealing and the active recrystallization of $TiO_2$ during air annealing. The decrease of carbon concentration by employing the two-step approach was supported by changes in the lattice parameters of $TiO_2$ and proven by X-ray photoelectron spectroscopy (XPS). The given study provides experimental evidence on how nanoscale carbon species in the $TiO_2$ heterojunction partner layer of a $Sb_2Se_3$ solar cell can affect the device's performance. By this approach, we generate complementary insights on how the quality of the main interface has an impact and can take a key role despite the optimized $Sb_2Se_3$ grain structure and orientation.

## Introduction

The field of thin film photovoltaics (PV) is booming at the moment as it is seeing remarkably fast progress in the development and optimization of new emerging

[a]*Department of Materials and Environmental Technology, Tallinn University of Technology, Ehitajate tee 5, 12616 Tallinn, Estonia. E-mail: nicolae.spalatu@taltech.ee*
[b]*Competence Centre Photovoltaics Berlin (PVcomB), Helmholtz-Zentrum Berlin für Materialen und Energie (HZB), Schwarzschildstraße 3, 12489 Berlin, Germany*

semiconductor absorber materials, such as thin sulfides,[1] chalcostibites,[2] chalcogenide perovskites,[3] nitrides,[4] and antimony chalcogenides.[5,6] These materials have attracted intensive thin film PV research of late because of the high abundance of their constituent elements in the Earth's crust and the non-toxicity of the chemical elements, which are combined with highly demanded material qualities, such as defect tolerance[6] and high chemical stability. Among these materials, Sb-chalcogenides, *e.g.*, $Sb_2Se_3$, $Sb_2S_3$, and $Sb_2(S,Se)_3$, have demonstrated great potential with a nascent track record of performance development. $Sb_2Se_3$ and $Sb_2S_3$ are both single-phase binary compounds with quasi-one-dimensional crystal structures, absorption coefficients of $>10^4$ $cm^{-1}$ (for energies above 1.5 eV)[7,8] and band gap energies of ~1.2 eV and ~1.7 eV,[9,10] respectively. Such optoelectronic properties are excellent for developing efficient thin film solar cell devices.

Despite a paucity of research, PV devices based on antimony chalcogenides have already reached cell power conversion efficiencies (PCEs) of around 10%.[11] As for $Sb_2Se_3$, the absorber material in the focus of the current study, absorbers deposited by close-spaced sublimation[12,13] and vapor transport[14] deposition techniques have produced devices with record PCEs ranging between 7–9%. Despite these achievements, there are several challenges that need to be overcome to harness the full potential of $Sb_2Se_3$ PV devices. Critical limitations include finding an optimal device structure,[15] optimization of $Sb_2Se_3$ growth,[6,12,13] identification of suitable heterojunction partner layers,[9,15,16] and development of post-deposition treatments and doping strategies.[17,18] Most of the R&D efforts in recent years have been focused on optimizing $Sb_2Se_3$ growth, in conjunction with a CdS heterojunction buffer layer, an established partner layer in CdTe,[19] CIGS,[20] and CZTS solar cells.[21] While the CdS buffer layer ($E_g \sim 2.5$ eV)[22] has been the preferred choice for a majority of research groups,[9,14,23] and has shown favorable band alignment with the $Sb_2Se_3$ absorber,[15] $TiO_2$ buffer layers ($E_g = 2.8$–$3.3$ eV)[24] have emerged as suitable and more stable alternatives to CdS buffer layers. Namely, chemical intermixing at the interface between CdS and $Sb_2Se_3$ has been reported in superstrate $Sb_2Se_3$/CdS PV devices, causing the formation of an interface layer, which acts like an electrostatic barrier that obstructs charge transfer and collection.[13] As for $TiO_2$ synthesis, spin coating (SC)[13] and ultrasonic spray pyrolysis (USP)[25] are common deposition techniques, especially for superstrate $Sb_2Se_3/TiO_2$ PV devices. The best superstrate $Sb_2Se_3/TiO_2$ solar cells have thus far demonstrated PCEs between 5–8%.[5,12]

Despite these promising results, there is ongoing research into various aspects of how the heterojunction between $TiO_2$ and $Sb_2Se_3$ can be improved. Since $Sb_2Se_3/TiO_2$ PV devices suffer from substantial $V_{OC}$ deficits, developing a strategy for $Sb_2Se_3/TiO_2$ interface engineering is of extreme importance for giving $Sb_2Se_3/TiO_2$ solar cells a further boost. One of the aspects in the $Sb_2Se_3/TiO_2$ interface engineering entails post-deposition treatment of the $TiO_2$ films after the films have been deposited by either UPS or SC chemical methods. Usually, such a treatment implies thermal annealing in air at 450–500 °C for 20–30 min,[10] with the main purpose of improving the crystallinity of the $TiO_2$ films. It is mostly accepted that for chemically deposited $TiO_2$ layers, air annealing at elevated temperatures causes residual organic components, which are inevitably present in the precursor solution, to be easily removed as a result of a pyrolysis process. However, in our recent study, we noticed that the pyrolysis process in the presence

of air at high temperatures might not be enough to purge the $TiO_2$ films of organic residuals, and to some extent, organic residuals may remain on the $TiO_2$ surface and could degrade the quality of the $Sb_2Se_3/TiO_2$ interface and curtail the performance of the device.[12] Hence, this finding served as a hypothesis, forming the basis of the subsequent study with the focus of systematically investigating the effects of different annealing procedures over a wide range of temperatures on the properties of the $TiO_2$ films and the performance of $Sb_2Se_3/TiO_2$ solar cells. With this approach, we aimed to screen the evolution of organic residues at the surface of USP-deposited $TiO_2$ films, gain an understanding of the kinetics of a vacuum annealing process for removing these organic residuals, and assess the overall impact of annealing on $Sb_2Se_3/TiO_2$ solar cell performance.

# Experimental

### Fabrication of superstrate configuration glass/FTO/$TiO_2$/$Sb_2Se_3$/Au thin film solar cells

The solar cells were fabricated according to the superstrate configuration. FTO-coated 2.3 mm thick glass with a surface resistivity of 7 $\Omega$ $sq^{-1}$ (provided by Sigma-Aldrich) was used as a substrate. USP $TiO_2$ films were deposited atop FTO at 340 °C using a precursor solution of a 1 : 4 ratio of titanium(IV) isopropoxide (TTIP) and acetylacetone (AcacH). The USP deposition was set in a way to keep a constant controllable $TiO_2$ thickness of 80–90 nm. In the next step, the $TiO_2$ films were divided into two sets and subjected to three different annealing procedures, described in the section below. After the annealing of $TiO_2$, a 1.3–1.5 μm thick $Sb_2Se_3$ absorber layer was deposited at 460 °C by CSS, following a previously described procedure.[26] 5 N granular $Sb_2Se_3$ (Sigma-Aldrich) was used as the source material for the absorber deposition. To complete the solar cell, an Au back contact was deposited *via* thermal evaporation.

### Post deposition annealing of USP $TiO_2$ films

After the deposition, the $TiO_2$ sets underwent three annealing procedures: (I) vacuum annealing only (labeled as "Vac"), (II) vacuum and subsequent air annealing (labeled as "Vac+Air"), and (III) air annealing only (labeled as "Air"); vacuum annealing of the USP $TiO_2$ films was carried out in a closed process tube with a diameter of 55 mm and a volume of 1500 mL. For this procedure, the process tube containing the samples was evacuated at room temperature (RT) and then introduced into a cylindrical furnace set at RT, to allow a slow thermal annealing process. The annealing temperature was varied in the 160–450 °C range in steps of $\Delta T = 50$ °C, and the annealing time was fixed at 60 min. The vacuum level in the process tube was maintained at $\sim 10^{-5}$ mbar, using a turbomolecular vacuum pump in a dynamic regime. Air annealing of the USP $TiO_2$ films was carried out in a pre-heated open process tube at 450 °C. The annealing time was fixed at 30 min, after which the tube was taken out from the furnace for rapid cooling at room temperature.

### Material and device characterization

X-ray diffraction (XRD) and scanning electron microscopy (SEM) were used to analyze the structural and morphological properties of the samples. XRD

characterization was carried out on a Rigaku Ultima IV diffractometer with Cu Kα radiation ($\lambda = 1.54$ Å, 40 kV, 40 mA). Rigaku PDXL software was used to analyze the XRD data. The following data cards were used: JCPDS 01-089-0821 for $Sb_2Se_3$, JCPDS 00-021-1272 for $TiO_2$ and JCPDS 01-077-0452 for FTO ($SnO_2$). A Zeiss HR-SEM MERLIN SEM with the GEMINI II column was used for the top and cross-sectional views of the structures. The XPS spectra were measured with a standard XPS laboratory system based on a nonmonochromatic X-ray source from SPECS with a Mg anode, providing an excitation energy of 1253.6 eV.[27] All XPS spectra were measured at room temperature at a pressure of $5 \times 10^{-6}$ Pa. The energy analyzer was calibrated by fixing the C 1s core level binding energy at 285.0 eV. AUTOLAB PGSTAT 30 and an Oriel class A solar simulator 91159A (100 mW $cm^{-2}$, AM1.5) were used for *J–V* characteristic measurements. In the EQE measurements, a 300 W xenon lamp and an SPM-2 Carl Zeiss-Jena monochromator were used at 30 Hz.

## Results and discussion

XRD and SEM techniques were used to analyze the structural properties of the as-deposited and annealed $TiO_2$ films. Fig. 1a and b show the XRD patterns of the $TiO_2$ films which underwent different annealing steps. It is observed that for the as-deposited $TiO_2$ film, the diffractogram does not show clearly distinguishable peaks related to the $TiO_2$ crystal structure, indicating that the layers contain a large amount of the amorphous phase. The amorphous phase is kept present in both the Vac+Air and Vac 160–250 °C annealing steps. For Vac+Air and Vac annealing in the range of 300–450 °C, all the $TiO_2$ films showed an anatase crystal structure (PDF: JCPDS 00-021-1272), with characteristic (101) and (200) peaks at 25.28° and 48.05°, respectively . These peaks are characteristic of anatase $TiO_2$ and have been previously reported for USP-deposited $TiO_2$ films.[28] To understand

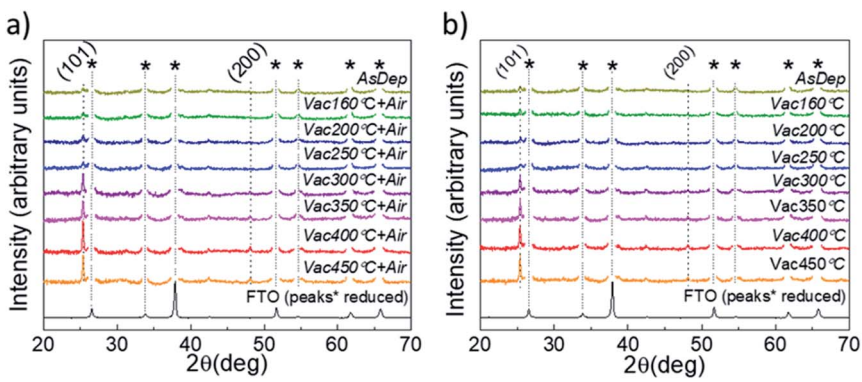


Fig. 1 XRD patterns of $TiO_2$ thin films (showing the characteristic (101) and (200) peaks of anatase $TiO_2$) deposited by USP onto FTO/glass substrates, before and after annealing procedures. (a) Vacuum annealing at the temperature range of 160–450 °C for 60 min, and subsequent air treatment at 450 °C for 30 min (labelled as VacT°+Air). (b) Vacuum annealing at 160–450 °C for 60 min (labeled as VacT°). For a better clarity of the diffractograms, the strong peak reflections related to FTO underlayer (marked with star symbols) were artificially reduced.

the effect of annealing conditions on the structural properties of $TiO_2$ layers, we further analyzed the changes in the crystallite sizes (Fig. 2d, e). As an overall trend, the crystallite size increases with the increase of the Vac+Air and Vac annealing temperatures. For the Vac+Air treatment (Fig. 2d), crystallites were ≈30 nm at low-$T$ (160–250 °C) annealing and ≈50 nm at high-$T$ (300–450 °C) annealing. In the case of the Vac annealing, the trend in crystallite size was slightly sharper, with ≈20 nm size at low-$T$ (160–250 °C) and ≈60 nm large crystallites after annealing at 450 °C (Fig. 2e).

Fig. 2a and b show the top-view SEM images of the $TiO_2$ samples before and after vacuum annealing at 160 °C and subsequent 450 °C air treatment, respectively. The cross-sectional view of the 160 °C vacuum annealed and 450 °C subsequent air treated $TiO_2$ layer is shown in Fig. 2c. As can be seen in Fig. 2a, the amorphous $TiO_2$ film consists of small grains and has quite a homogeneous distribution. After annealing, the films are more compact with well-sintered grains (Fig. 2b) and the thickness is reasonably uniform (Fig. 2c). It is important to note that the $TiO_2$ films kept the same morphology (shown in Fig. 2b) independent of the Vac+Air, Vac, or Air annealing at 450 °C. It is also worth mentioning that from the UV-Vis measurements (Tauc plots, not shown), the band gap value of $TiO_2$ was determined to be $E_g$ ~3.3 eV and no changes in this value have been observed, independent of either Vac+Air, Vac, or air annealing at 450 °C.

Based on the above XRD and SEM results, it can be concluded that there were no noticeable differences in the properties of $TiO_2$ films when annealed with different Vac+Air, Vac, or Air conditions. A systematic increasing trend in the crystallite size with the increase of annealing temperature was expected, however looking from the perspective of the organic impurity incorporation into the lattice of $TiO_2$ films, the evolution in the lattice parameters of the annealed films was

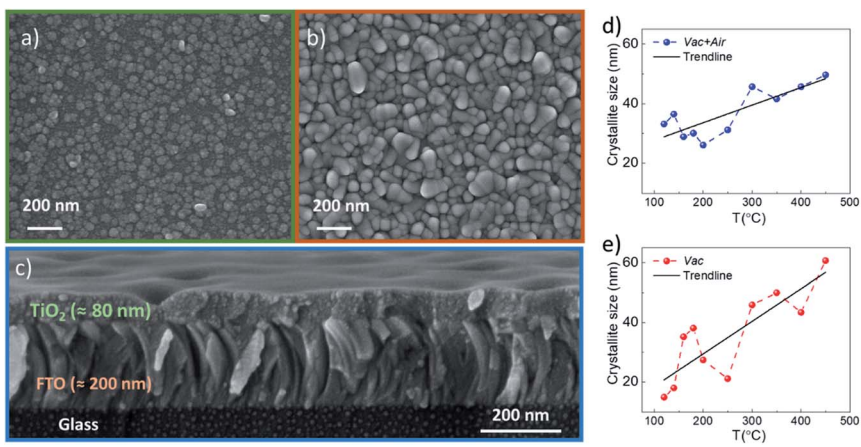


Fig. 2 (a and b) Top view SEM images of USP-deposited $TiO_2$ after a 160 °C vacuum annealing step (Vac) and after 160 °C vacuum and subsequently 450 °C air annealing steps (Vac+Air), respectively. (c) Cross-sectional view of the $TiO_2$ layer after 160 °C vacuum and subsequently 450 °C air annealing steps (Vac+Air). (d and e) Evolution of the crystallite size of vacuum and subsequently air annealed (labeled as Vac+Air) and vacuum annealed only (labeled as Vac) $TiO_2$ films.

analyzed. The lattice parameters of anatase $TiO_2$ correspond to tetragonal crystal lattice with $a = b \neq c$ and the values for the Vac160 °C annealed films were between $a = b \sim 3.68$–$3.75$ and $c \sim 9.50$–$9.52$ Å. A small but systematic gradual decrease of the lattice parameters along all the $a$, $b$ and $c$ axes, from $a = b \sim 3.75$, $c = 9.51$ Å in the Vac160°C annealed films to $a = b \sim 3.80$, $c = 9.55$ Å in the Vac450°C treated layers was observed. An explanation for such a phenomenon can be related to the decrease in organic species in the $TiO_2$ lattice by a gradual increase of the Vac annealing temperature. A plausible hypothesis related to the presence of possible organic species in the $TiO_2$ lattice is the presence of carbon impurities.[29,30] Such a scenario is quite possible considering the fact that the USP $TiO_2$ precursor solution contains TTIP and AcacH in the ratio of 1 : 4, where the AcacH is a good source of carbon contamination. During the USP deposition process at 340 °C in air, the carbon from AcacH could incorporate into the $TiO_2$ lattice. Incorporation of carbon atoms into the lattice of anatase $TiO_2$ could occur through a substitutional mechanism at the oxygen sites.[29] At the same time, the carbon species are present on the surface of the $TiO_2$.[31] The concentration of carbon and related organic species seems to be $\leq 10^{19}$ $cm^{-3}$ (*i.e.* ≤0.01 at%), which is below the detection limit of classical XRD and EDX techniques. In this direction, employment of the XPS technique can provide a more in-depth analysis of the residual species at the $TiO_2$ surface. However, the large number of samples processed with various annealing conditions would imply intensive and time-consuming XPS measurement efforts. Thus, as a next stage, a large set of $Sb_2Se_3/TiO_2$ solar cells were fabricated with $TiO_2$ annealed at various conditions, and the impact of the treatment on the device performance was analyzed. With this approach, we attempted to identify the optimal $TiO_2$ annealing conditions which would allow reasonable device efficiency and, thus, to select a reasonable set of $TiO_2$ samples for the analysis of carbon species by XPS. Fig. 3 shows the solar cell parameters for $Sb_2Se_3$ devices employing a $TiO_2$ buffer layer that underwent either Air, Vac+Air, or Vac annealing.

It is clear from Fig. 3 that the devices annealed according to the Vac+Air approach gained a significant boost in performance over devices that were subject to just one of the two other annealing procedures. All *J–V* parameters showed higher values for a combined Vac+Air procedure in the temperature range of 160–300 °C, with the Vac+Air procedure carried out at 160 °C enabling the best device performance of 4.7%. The *J–V* characteristics and EQE spectral response of the representative 4.7% efficient device are shown in Fig. 4a and b. The increase of the annealing temperature beyond 160 °C in the Vac+Air procedure caused all solar cell parameters to slightly worsen. Also important to note is the fact that the Vac+Air annealing of $TiO_2$ layers at temperatures in the range of 350 to 450 °C causes devices to produce lower $J_{SC}$ values than devices with Vac annealed $TiO_2$ layers (Fig. 3). Considering the differences in the solar cell efficiencies (Fig. 3), one could emphasize that the grain structure and texture of the $Sb_2Se_3$ absorber films deposited on either Vac, Vac+Air, or Air annealed $TiO_2$ should be reflected in the final device performance. Looking at the top- and cross-sectional view SEM images of $Sb_2Se_3$ absorber films deposited onto Vac160°C+Air (Fig. 5a and b) and Vac450°C+Air (Fig. 5c and d) annealed $TiO_2$, no detectable changes in the grain morphology of the absorber were observed. Independent of the $TiO_2$ annealing procedure, the absorber growth follows a similar morphology of columnar sintered grains (Fig. 5b and d).

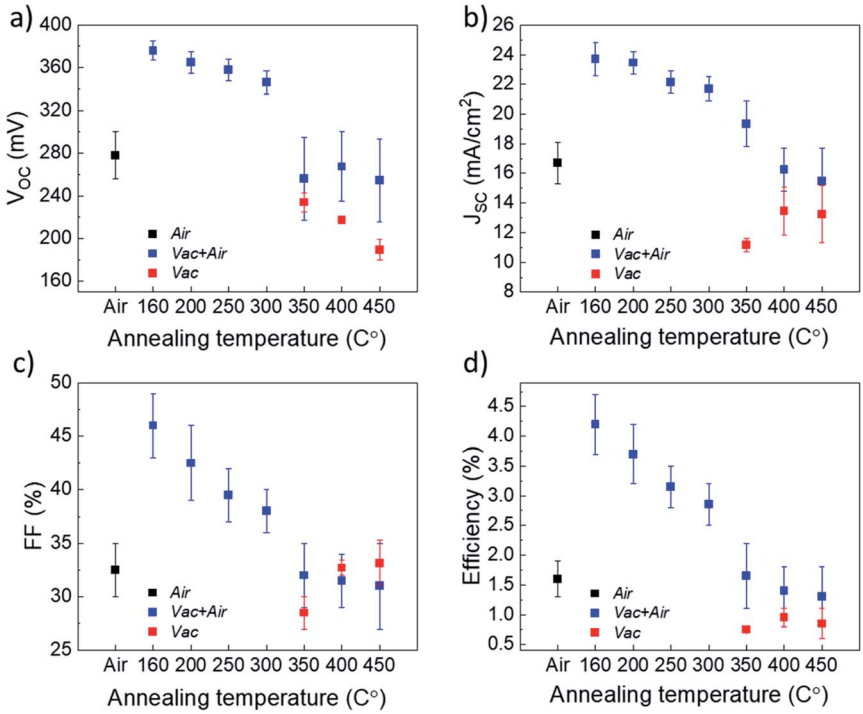


Fig. 3 $J$–$V$ parameters, including (a) open-circuit voltage – $V_{OC}$, (b) short-circuit current density – $J_{SC}$, (c) fill factor – FF and (d) efficiency of $TiO_2/Sb_2Se_3$ devices with different $TiO_2$ annealing conditions.

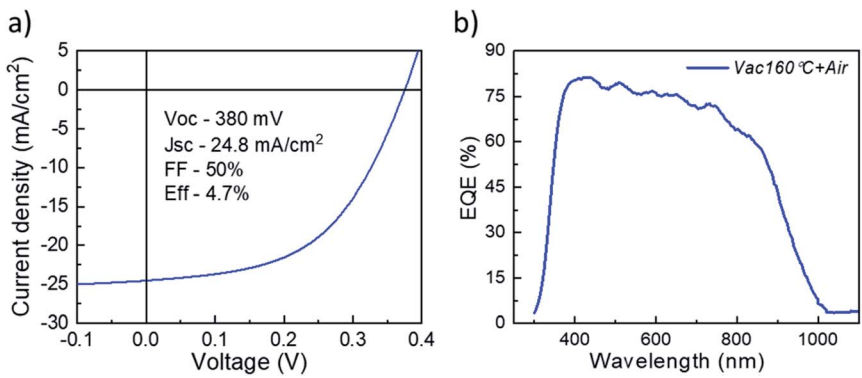


Fig. 4 (a) $J$–$V$ characteristics and (b) EQE spectral response of the representative 4.7% efficiency device.

Analysis of the XRD patterns of the $Sb_2Se_3$ absorber deposited onto Vac+Air and Vac annealed $TiO_2$ layers (Fig. 6a and b) and the related texture coefficients (Fig. 6c and d) reveals that independent of the $TiO_2$ annealing, the absorber exhibits preferential orientation along the (211), (221) and (002) planes.

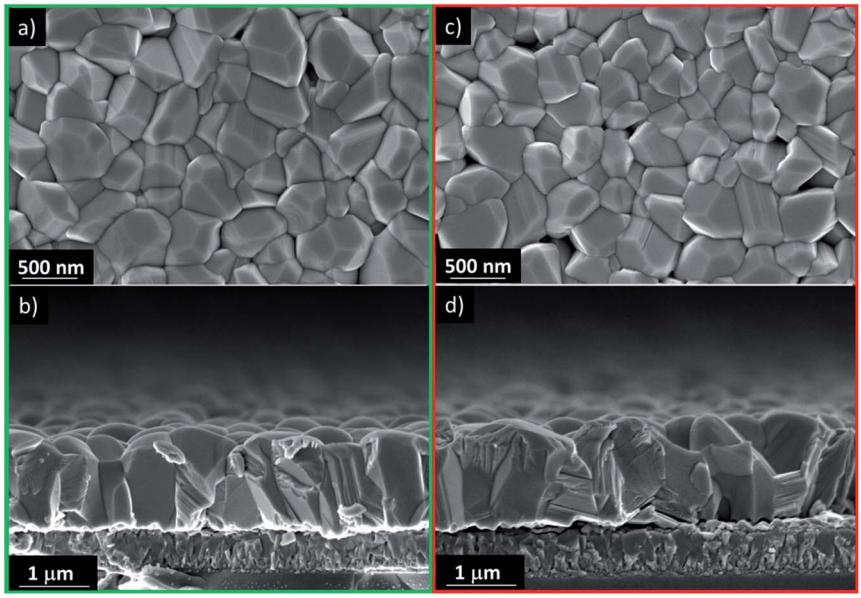


Fig. 5 Top-and cross-sectional view SEM images of CSS $Sb_2Se_3$ absorber films deposited at 460 °C onto $TiO_2$/FTO/glass stacked substrates, with (a and b) 160 °C vacuum and consequent 450 °C air annealed $TiO_2$ and (c and d) 450 °C vacuum and consequent 450 °C air annealed $TiO_2$ layers.

These peaks are characteristic of the orthorhombic $Sb_2Se_3$ crystal structure (PDF card no. 01-089-0821) and match well with those reported in the literature for the $Sb_2Se_3$ absorber deposited by the CSS and VTD techniques.[32–35] Although there could be other changes at the nanoscale of the absorber (grain interior to grain boundaries), these results indicate that the quality of the main $Sb_2Se_3$–$TiO_2$ interface (which is determined by the annealing approach of $TiO_2$) is the main parameter which affects the solar cell performance in Fig. 3. The optimum efficiency point found for 160 °C $TiO_2$ vacuum annealing may be explained through the combined effect of reduced carbon content in the vacuum annealing step and oxygen-included recrystallization of the film during the following 450 °C air annealing step. A low carbon content at the $Sb_2Se_3$–$TiO_2$ main interface implies an improved heterojunction formation (and, probably, a lower concentration of the interface defect states), resulting in an increased performance of the solar cell (Fig. 3).

So far, our results indicate that the vacuum annealing of $TiO_2$ can be a suitable processing step for decreasing the concentration of organic residual species in $TiO_2$ and, by this, to improve the heterojunction quality and cell efficiency. However, the treatment needs to be performed at a moderate temperature ($\leq$200 °C) so as to keep the $TiO_2$ grain sizes small enough for their active recrystallization in the subsequent air annealing step at 450 °C. On the other hand, the low solar cell efficiency obtained with only Vac annealed $TiO_2$ (*i.e.*, without subsequent 450 °C air treatment) indicates the necessity of oxygen-rich conditions during the recrystallization of USP deposited $TiO_2$.

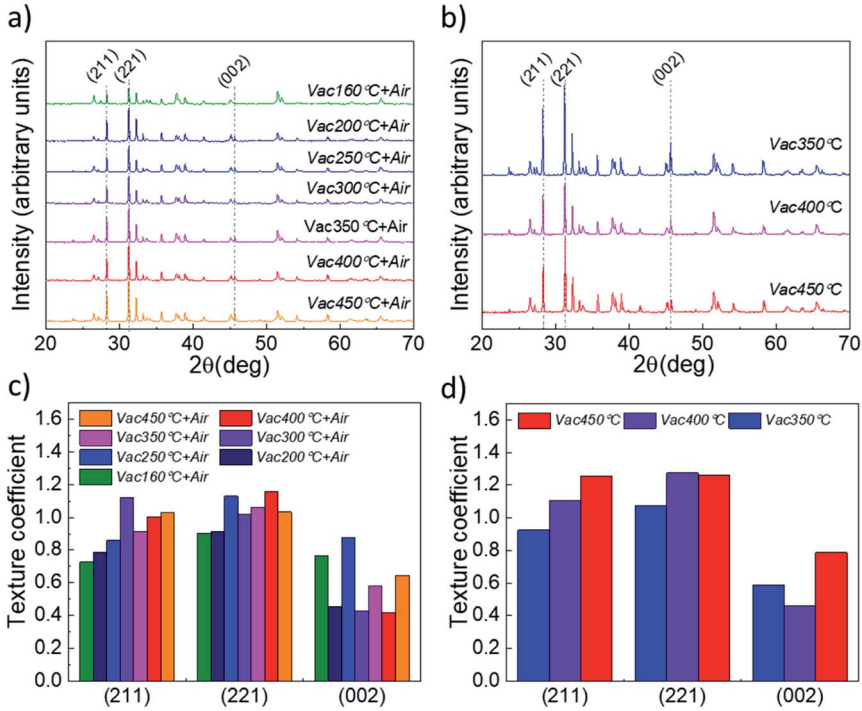


Fig. 6 XRD patterns of CSS $Sb_2Se_3$ absorber films deposited at 460 °C onto $TiO_2$/FTO/glass stacked substrates, with (a) vacuum and subsequent air annealed (Vac+Air) $TiO_2$ and (b) vacuum annealed only (Vac) $TiO_2$ layers. Related texture coefficients (TC) for (c) vacuum and subsequent air annealed (Vac+Air) and (d) vacuum annealed (Vac) films, calculated from the integrated intensity ratios (using the Harris formula[46]) for the dominant miller planes of $Sb_2Se_3$.

To provide support for the above statements, especially on the concentration of carbon species at the $TiO_2$ surface, we further analyzed the annealed $TiO_2$ films by XPS. The XPS spectra were registered from the surface of ~80 nm thick USP $TiO_2$ films deposited at 340 °C onto FTO/glass substrates. Since no distinguishable differences were observed between the spectra of the as deposited and annealed $TiO_2$, only one survey spectrum of the as-deposited $TiO_2$ film is illustrated in Fig. 7a. The binding energy (BE) values, as well as the shape of the Ti $2p_{3/2}$ and O 1s core level peaks (not shown here), are characteristics of single-phase anatase $TiO_2$ films.[28] Emission of the Sn $3d_{5/2}$ core level from the underlying FTO substrate is registered only in the case of the as-deposited film and can be related to the presence of some pinholes in the $TiO_2$ film. No secondary phases were revealed in any of the as deposited or annealed $TiO_2$ films, supporting the above-mentioned XRD results (Fig. 1).

To clarify the evolution of carbon impurities at the surface of the annealed $TiO_2$ films, we analyzed the C 1s core level emission. We cannot quantify the air contamination of the measured surfaces but, keeping in mind that all the $TiO_2$ samples spent the same time in air from the UPS until the XPS analysis, we assume that a similar amount of carbon species from the air contamination is

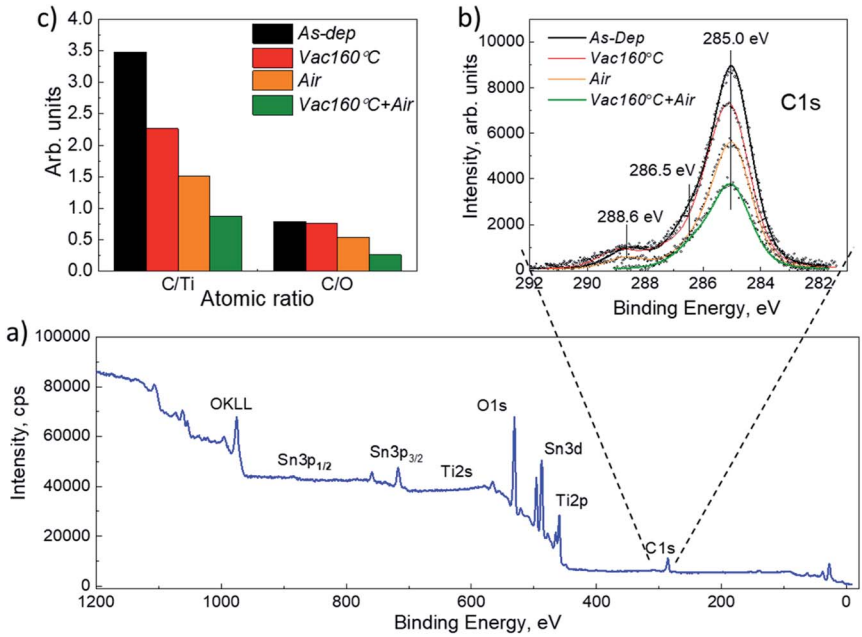


Fig. 7 (a) XPS survey spectrum of $TiO_2$ films deposited by USP at 340 °C onto FTO/glass substrates. (b) C 1s core level from the as deposited (labelled as As-dep), 160 °C vacuum annealed (labelled as Vac160°C), 450 °C air annealed (labelled as Air), 160 °C vacuum and subsequent 450 °C air annealed (Vac160°C+Air) $TiO_2$ films. (c) Calculated atomic ratios C/Ti and C/O for the related samples.

present on all analyzed samples and the differences in the C 1s signal can be attributed to the fluctuation of other carbon species from the near surface bulk of the $TiO_2$ film. The C 1s peak contains three features at BE values of 285.0 eV, 286.5 eV, and 288.6 eV (Fig. 7b). The highest peak located at 285.0 eV originates from the C=C bond. Peaks with the BE values 286.5 eV and 288.6 eV represent the oxygen-bound species C–O and Ti–O–C bonds, respectively.[36] These peaks, and especially the one at 288.6 eV, confirm the incorporation of carbon into the $TiO_2$ lattice.[37] Therefore, we consider the C 1s emission at 288.6 eV as evidence of so-called organic residuals of the USP precursor solution (TTIP complex, together with oxygen, and carbon from AcacH) and analyze how they are affected by the annealing of $TiO_2$.

Fig. 7b and Table 1 show that the as-deposited $TiO_2$ films contain the most intense C 1s emission at 288.6 eV and vacuum (Vac) annealing at 160 °C slightly decreased it. Such a low annealing temperature seems to be insufficient for a significant reduction of carbon. An air treatment at 450 °C further reduced the concentration of the carbon, however, the lowest intensity of 288.6 eV emission was observed for the combination of the two steps, Vac160°C and subsequent Air 450 °C annealing of $TiO_2$ (Fig. 7). Interestingly, in the case of the Vac+Air treated samples, the concentration of oxygen was found to be much higher compared with those from the Vac annealed samples (63.5 at% *vs.* 52.5 at%, Table 1).

The XPS results prove that the organic residuals of the USP precursor solution are not easily removed as vapors of $H_2O$ and CO and $CO_2$ gas at the stage of the

Table 1 Relative atomic concentration of elements (from natural spectra of C 1s, N 1s, O 1s, and Ti $2p_{3/2}$ core levels) in $TiO_2$ thin films before and after: 160 °C vacuum, 450 °C air, 160 °C vacuum, and subsequent 450 °C air annealing steps

| Sample | C 1s, at% | N 1s, at% | O 1s, at% | Ti $2p_{3/2}$, at% |
|---|---|---|---|---|
| As-dep | 38.3 | 1.8 | 48.3 | 11.8 |
| Vac | 36 | 0.6 | 47.6 | 15.9 |
| Air | 28.2 | 0.6 | 52.5 | 18.7 |
| Vac+Air | 16.3 | 1.5 | 63.5 | 18.8 |

USP deposition at 340 °C and during post-deposition air treatment at 450 °C. A few recent studies from the photocatalysis field have shown the presence of carbon species in USP $TiO_2$ films after air annealing at temperatures ≥500 °C and after additional ultraviolet treatments.[38]

Moreover, the carbon was found to be beneficial for the photocatalytic performance of $TiO_2$.[39] The same TTIP–AcacH based precursor solution is widely used for the spin coating and USP deposition of planar $TiO_2$ films as an electron transport layer in perovskite solar cells.[40,41] In particular, for $TiO_2$ based perovskites, a single step air treatment at 450–500 °C is a well-established annealing step and there is little to no impact of the AcacH concentration (over a wide range from 1 : 10 to 1 : 20 TTIP : AcacH ratios) on the perovskite device performance.[42,43] Our results instead bring experimental evidence that the USP precursor and annealing procedures for $TiO_2$ strongly impact the efficiency of $Sb_2Se_3/TiO_2$ solar cells. Based on XPS data (and changes in the lattice parameters of $TiO_2$), we show that the residual carbon species (Fig. 7b) play an important role in the composition of the surface and bulk defects in $TiO_2$. This effect is then translated into the quality of the $Sb_2Se_3$–$TiO_2$ heterointerface formation and subsequently has a great impact on the final device performance. We demonstrate that vacuum annealing could be a suitable technological approach to decrease the concentration of carbon species in $TiO_2$ films and, by this, to improve the performance of $Sb_2Se_3$ solar cell efficiency. However, more research efforts are required to understand the correlation between the USP precursor solution, residual organic species, and $TiO_2$ surface defects and, thus, their impact on the $TiO_2$–$Sb_2Se_3$ interface, related interface defect states, and final device performance. In this direction, a combination of advanced characterization methods, such as scanning transmission electron microscopy (STEM)[44] and transient SPV spectroscopy,[45] could be suitable techniques to gain in-depth insights into the impact of nanoscale carbon species on GBs electronic properties in $TiO_2$ and passivation of the electronic traps at the main interface.

## Conclusions

In this work, we systematically study the impact of $TiO_2$ annealing conditions on the performance of $Sb_2Se_3/TiO_2$ thin film solar cells. The results were compared for three annealing variations: vacuum annealing only at 160–450 °C, two-step vacuum annealing at 160–450 °C followed by a subsequent 450 °C air treatment, and 450 °C air treatment only. XRD and SEM analysis showed improved

structural properties of the $TiO_2$ when a two-step annealing was applied. We showed that vacuum annealing can be a suitable technological approach to decrease the concentration of organic residues in $TiO_2$ films. Changes in the lattice parameters of annealed $TiO_2$ indicated the processes taking place inside the crystalline lattice of the $TiO_2$ films and were connected with the removal of residual species. The annealing conditions do not affect the grain structure of the $Sb_2Se_3$ absorber films but significantly impact the final device performance. The employment of one step $TiO_2$ vacuum annealing has a detrimental impact on the cell efficiency. Vacuum annealing at 160 °C followed by subsequent 450 °C air treatment led to a 4.7% device performance. This was explained by achieving an optimal balance between the removal of carbon content during vacuum annealing and the active recrystallization of $TiO_2$ during air annealing. The decrease of the carbon concentration by employing the two-step approach was proven by XPS. Our findings pave a solid platform for further research investigations on the impact of organic residues in chemically processed $TiO_2$, including optimization of post deposition treatments for efficient $Sb_2Se_3$ solar cells.

## Author contributions

Mykhailo Koltsov: conceptualization, data curation, formal analysis, methodology, software, visualization, writing – original draft. Robert Krautmann: software, visualization, writing – review & editing. Atanas Katerski: formal analysis, writing – review & editing. Natalia Maticiuc: formal analysis, writing – review & editing, validation. Malle Krunks: formal analysis, validation. Ilona Oja Acik: validation, project administration, funding acquisition. Nicolae Spalatu: conceptualization, formal analysis, methodology, supervision, visualization, writing – review & editing, validation and funding acquisition.

## Conflicts of interest

There are no conflicts to declare.

## Acknowledgements

This study was funded by the Estonian Research Council project PRG627 “Antimony chalcogenide thin films for next-generation semi-transparent solar cells applicable in electricity producing windows”, the Estonian Research Council project PSG689 “Bismuth Chalcogenide Thin-Film Disruptive Green Solar Technology for Next Generation Photovoltaics”, the Estonian Centre of Excellence project TK141 (TAR16016EK) “Advanced materials and high-technology devices for energy recuperation system”, and the EU H2020 program under the ERA Chair project 5GSOLAR grant agreement no. 952509.

## Notes and references

1 N. Spalatu, J. Hiie, R. Kaupmees, O. Volobujeva, J. Krustok, I. O. Acik and M. Krunks, *ACS Appl. Mater. Interfaces*, 2019, **11**, 17539–17554.
2 N. C. Miller and M. Bernechea, *APL Mater.*, 2018, **6**, 084503.
3 D. Tiwari, O. S. Hutter and G. Longo, *J. Phys.: Energy*, 2021, **3**, 034010.

4 A. Zakutayev, *Rapid Development of Disruptive Photovoltaic Technologies*, 2019.
5 T. D. C. Hobson, L. J. Phillips, O. S. Hutter, H. Shiel, J. E. N. Swallow, C. N. Savory, P. K. Nayak, S. Mariotti, B. Das, L. Bowen, L. A. H. Jones, T. J. Featherstone, M. J. Smiles, M. A. Farnworth, G. Zoppi, P. K. Thakur, T.-L. Lee, H. J. Snaith, C. Leighton, D. O. Scanlon, V. R. Dhanak, K. Durose, T. D. Veal and J. D. Major, *Chem. Mater.*, 2020, **32**, 2621–2630.
6 R. Krautmann, N. Spalatu, R. Gunder, D. Abou-Ras, T. Unold, S. Schorr, M. Krunks and I. Oja Acik, *Sol. Energy*, 2021, **225**, 494–500.
7 I. Caño, P. Vidal-Fuentes, L. Calvo-Barrio, X. Alcobé, J. M. Asensi, S. Giraldo, Y. Sánchez, Z. Jehl, M. Placidi, J. Puigdollers, V. Izquierdo-Roca and E. Saucedo, *ACS Appl. Mater. Interfaces*, 2022, **14**, 11222–11234.
8 C. Chen, W. Li, Y. Zhou, C. Chen, M. Luo, X. Liu, K. Zeng, B. Yang, C. Zhang, J. Han and J. Tang, *Appl. Phys. Lett.*, 2015, **107**, 043905.
9 Z. Li, X. Liang, G. Li, H. Liu, H. Zhang, J. Guo, J. Chen, K. Shen, X. San, W. Yu, R. E. I. Schropp and Y. Mai, *Nat. Commun.*, 2019, **10**, 1.
10 J. S. Eensalu, A. Katerski, E. Kärber, L. Weinhardt, M. Blum, C. Heske, W. Yang, I. Oja Acik and M. Krunks, *Beilstein J. Nanotechnol.*, 2019, **10**, 2396–2409.
11 Y. Zhao, S. Wang, C. Jiang, C. Li, P. Xiao, R. Tang, J. Gong, G. Chen, T. Chen, J. Li and X. Xiao, *Adv. Energy Mater.*, 2022, **12**, 2103015.
12 N. Spalatu, R. Krautmann, A. Katerski, E. Karber, R. Josepson, J. Hiie, I. O. Acik and M. Krunks, *Sol. Energy Mater. Sol. Cells*, 2021, **225**, 111045.
13 L. J. Phillips, C. N. Savory, O. S. Hutter, P. J. Yates, H. Shiel, S. Mariotti, L. Bowen, M. Birkett, K. Durose, D. O. Scanlon and J. D. Major, *IEEE J. Photovolt.*, 2019, **9**, 544–551.
14 X. Wen, C. Chen, S. Lu, K. Li, R. Kondrotas, Y. Zhao, W. Chen, L. Gao, C. Wang, J. Zhang, G. Niu and J. Tang, *Nat. Commun.*, 2018, **9**, 1.
15 H. Shiel, O. S. Hutter, J. E. N. Swallow, L. A. Jones, T. J. Featherstone, M. J. Smiles, P. K. Thakur, L. J. Phillips, K. Durose, J. D. Major, V. R. Dhanak, T.-L. Lee and T. D. Veal, *Band Alignment Measurements of $Sb_2Se_3$ Solar Cells Using HAXPES*, 2015.
16 L. Wang, D. B. Li, K. Li, C. Chen, H. X. Deng, L. Gao, Y. Zhao, F. Jiang, L. Li, F. Huang, Y. He, H. Song, G. Niu and J. Tang, *Nat. Energy*, 2017, **2**, 17046.
17 V. Kumar, E. Artegiani, P. Punathil, M. Bertoncello, M. Meneghini, F. Piccinelli and A. Romeo, *ACS Appl. Energy Mater.*, 2021, **4**, 12479–12486.
18 A. Stoliaroff, A. Lecomte, O. Rubel, S. Jobic, X. H. Zhang, C. Latouche and X. Rocquefelte, *ACS Appl. Energy Mater.*, 2020, **3**, 2496–2509.
19 T. Potlog, N. Spalatu, N. Maticiuc, J. Hiie, V. Valdna, V. Mikli and A. Mere, *Phys. Status Solidi A*, 2012, **209**, 272–276.
20 J. Ramanujam, D. M. Bishop, T. K. Todorov, O. Gunawan, J. Rath, R. Nekovei, E. Artegiani and A. Romeo, *Prog. Mater. Sci.*, 2020, **110**, 100619.
21 J. Andrade-Arvizu, R. F. Rubio, V. Izquierdo-Roca, I. Becerril-Romero, D. Sylla, P. Vidal-Fuentes, Z. J. Li-Kao, A. Thomere, S. Giraldo, K. Tiwari, S. Resalati, M. Guc and M. Placidi, *ACS Appl. Mater. Interfaces*, 2022, **14**, 1177–1186.
22 N. Maticiuc, N. Spalatu, V. Mikli and J. Hiie, in *Applied Surface Science*, Elsevier B.V., 2015, vol. 350, pp. 14–18.
23 Y. Zhou, Y. Li, J. Luo, D. Li, X. Liu, C. Chen, H. Song, J. Ma, D. J. Xue, B. Yang and J. Tang, *Appl. Phys. Lett.*, 2017, **111**, 013901.
24 U. Diebold, *Surf. Sci. Rep.*, 2003, **48**, 53–229.

25 J. S. Eensalu, A. Katerski, E. Kärber, I. O. Acik, A. Mere, M. Krunks, J. S. Eensalu, A. Katerski, E. Kärber, I. O. Acik, A. Mere and M. Krunks, *Beilstein J. Nanotechnol.*, 2019, **10**, 198–210.
26 N. Spalatu, R. Krautmann, A. Katerski, E. Karber, R. Josepson, J. Hiie, I. O. Acik and M. Krunks, *Sol. Energy Mater. Sol. Cells*, 2021, **225**, 111045.
27 N. Maticiuc, T. Kodalle, J. Lauche, R. Wenisch, T. Bertram, C. A. Kaufmann and I. Lauermann, *Thin Solid Films*, 2018, **665**, 143–147.
28 I. Dundar, M. Krichevskaya, A. Katerski and I. O. Acik, *R. Soc. Open Sci.*, 2019, **6**, 181578.
29 J.-C. Lee, A.-I. Gopalan, G. Saianand, K.-P. Lee and W.-J. Kim, *Nanomaterials*, 2020, **10**, 456.
30 M. Reticcioli, I. Sokolović, M. Schmid, U. Diebold, M. Setvin and C. Franchini, *Phys. Rev. Lett.*, 2019, **122**, 016805.
31 U. Diebold, *Surf. Sci. Rep.*, 2003, **48**, 53–229.
32 Z. Li, X. Liang, G. Li, H. Liu, H. Zhang, J. Guo, J. Chen, K. Shen, X. San, W. Yu, R. E. I. Schropp and Y. Mai, *Nat. Commun.*, 2019, **10**, 1.
33 X. Wen, C. Chen, S. Lu, K. Li, R. Kondrotas, Y. Zhao, W. Chen, L. Gao, C. Wang, J. Zhang, G. Niu and J. Tang, *Nat. Commun.*, 2018, **9**, 1.
34 A. Chirilă, P. Reinhard, F. Pianezzi, P. Bloesch, A. R. Uhl, C. Fella, L. Kranz, D. Keller, C. Gretener, H. Hagendorfer, D. Jaeger, R. Erni, S. Nishiwaki, S. Buecheler and A. N. Tiwari, *Nat. Mater.*, 2013, **12**, 1107–1111.
35 J. Yang, Y. Lai, Y. Fan, Y. Jiang, D. Tang, L. Jiang, F. Liu and J. Li, *RSC Adv.*, 2015, **5**, 85592–85597.
36 Y. Zhang, Z. Zhao, J. Chen, L. Cheng, J. Chang, W. Sheng, C. Hu and S. Cao, *Appl. Catal., B*, 2015, **165**, 715–722.
37 R. Klaysri, M. Ratova, P. Praserthdam and P. Kelly, *Nanomaterials*, 2017, **7**, 113.
38 I. Dundar, M. Krichevskaya, A. Katerski, M. Krunks and I. O. Acik, *Catalysts*, 2019, **9**, 915.
39 J. Spiridonova, A. Mere, M. Krunks, M. Rosenberg, A. Kahru, M. Danilson, M. Krichevskaya and I. Oja Acik, *Catalysts*, 2020, **10**, 1011.
40 J. Sun, A. R. Pascoe, S. Meyer, Q. Wu, E. della Gaspera, S. R. Raga, T. Zhang, A. Nattestad, U. Bach, Y.-B. Cheng and J. J. Jasieniak, *Sol. Energy*, 2019, **188**, 697–705.
41 A. Möllmann, D. Gedamu, P. Vivo, R. Frohnhoven, D. Stadler, T. Fischer, I. Ka, M. Steinhorst, R. Nechache, F. Rosei, S. G. Cloutier, T. Kirchartz and S. Mathur, *Appl. Catal., B*, 2019, **21**, 1801196.
42 K. Wojciechowski, M. Saliba, T. Leijtens, A. Abate and H. J. Snaith, *Energy Environ. Sci.*, 2014, **7**, 1142–1147.
43 L. Kegelmann, C. M. Wolff, C. Awino, F. Lang, E. L. Unger, L. Korte, T. Dittrich, D. Neher, B. Rech and S. Albrecht, *ACS Appl. Mater. Interfaces*, 2017, **9**, 17245–17255.
44 J. A. Quirk, B. Miao, B. Feng, G. Kim, H. Ohta, Y. Ikuhara and K. P. McKenna, *Nano Lett.*, 2021, **21**, 9217–9223.
45 Th. Dittrich, L. E. Valle Rios, S. Kapil, G. Gurieva, N. Rujisamphan and S. Schorr, *Appl. Phys. Lett.*, 2017, **110**, 023901.
46 H. J. Bunge, *Textures Microstruct.*, 1997, **29**, 1–26.